DOI: 10.3847/1538-4357/ad479e
Typeset using LaTeX default style in AASTeX631

Azimuthal Size Scales of Solar Wind Periodic Density Structures

Simone Di Matteo [1,2] Christos Katsavrias [2,3] Larry Kepko [2] and Nicholeen M. Viall [2]

[1] *Physics Department, The Catholic University of America, Washington, DC, USA*
[2] *NASA-Goddard Space Flight Center, Greenbelt, MD, USA*
[3] *Department of Physics, National and Kapodistrian University of Athens, Athens, Greece*

(Accepted May 2, 2024)

ABSTRACT

Periodic Density Structures (PDSs) are quasi-periodic variations of solar wind density ranging from a few minutes to a few hours. PDSs advect with the solar wind and have radial length scales (L_x) of tens to several thousand Mm, thus belonging to the class of "mesoscale structures". Current interplanetary multi-spacecraft observations are not at spatial separations capable of directly measuring the 3D size scale of PDSs or other mesoscale structures. Instead, previous investigations estimated characteristic spatial scales in solar wind parameters using cross-correlation and/or coherence analysis applied to multi-spacecraft observations. For solar wind density and interplanetary magnetic field (IMF) intensity, the reported size scales perpendicular to the Sun-Earth line (L_y) ranged between ≈30 and ≈200 Earth Radii (R_E). Here, we implemented a similar approach on the same parameters but focused on high density slow solar wind intervals with PDSs observed by the Wind and ARTEMIS-P1 spacecraft. Additionally, this is the first statistical study of the IMF intensity periodicities in relation to PDSs. We identified intervals in which the two spacecraft observed the same periodicity obtaining two PDS groups based on their radial length scale: L_{x1} ≈86 R_E and L_{x2} ≈35 R_E. Then, we classified the events based on the periodic variations' coherence level. Reproducing the results with simulations of the PDSs' transit, we inferred the L_y order of magnitudes for the two PDS groups: L_{y1} ≈340 R_E and L_{y2} ≈187 R_E. Knowing the PDSs' size scales is fundamental to constrain models aimed at reproducing these structures and is critical to better understand the PDS-magnetosphere coupling.

Keywords: Interplanetary physics (827); Slow solar wind (1873); Solar coronal transients (312); Interplanetary turbulence (830); Planetary magnetospheres (997)

1. INTRODUCTION

Periodic density structures (PDSs) are a particular constituent of the ambient solar wind (Kepko et al. 2020). Quasi-periodic solar wind density variations have been reported in remote sensing observations of the Sun (Viall et al. 2008; Viall & Vourlidas 2015; Sánchez-Díaz et al. 2017; Alzate et al. 2021; Ventura et al. 2023; Poirier et al. 2023) and in situ observations from 0.3 to 1.0 AU (Kepko et al. 2016; Di Matteo et al. 2019b; Gershkovich et al. 2022; Gershkovich et al. 2023). The radial length scales of PDSs have been extensively investigated through case studies (Viall et al. 2010; Di Matteo et al. 2019a) and statistical analysis (Viall et al. 2008; Kepko et al. 2020). PDSs advect with the solar wind and have radial length scales (L_x) of tens to several thousand Mm. However, there is still an unclear understanding of their 3D extension. While remote sensing observations provide some insights (Viall et al. 2010; Sánchez-Díaz et al. 2017; DeForest et al. 2018), they are limited to the plane-of-sky.

Inference of characteristic size scales of solar wind coherent structures, in the range of the PDS scales, are mostly based on time series auto-correlation analysis (single spacecraft) or cross-correlation and/or coherence analysis (multi-spacecraft). Early investigations based on correlation between the interplanetary magnetic field (IMF) at spacecraft

Corresponding author: Simone Di Matteo
simone.dimatteo@nasa.gov

pairs reported scales along the direction perpendicular to the Sun-Earth line of ≈80 R_E (Chang & Nishida 1973) and ≈90 R_E (Crooker et al. 1982). Analysis of solar wind plasma flux from IMP 8, Wind, and INTERBALL-1 showed an almost constant correlation up to X_{GSE} ≈250 R_E (Paularena et al. 1998; Dalin et al. 2002) and an indication of a dependence on spacecraft separations along the Y_{GSE} direction with an extrapolated e-folding scale of ≈600–1000 R_E (Dalin et al. 2002). Higher correlation values are typically related to intervals manifesting higher standard deviation in variations of both density (Paularena et al. 1998; Dalin et al. 2002) and IMF (Crooker et al. 1982). Collier et al. (2000) advanced the idea of the "two length scale medium" based on IMF observations: a short scale length (many 10s of R_E) representing correlation decay along a solar wind parcel and a larger scale length (on the order of ≈100 R_E) over which two spacecraft are unlikely to even observe the same solar wind parcel. Richardson & Paularena (2001) defined characteristic scale sizes as the distance over which the correlation function falls by 10 % and reported radial/perpendicular (with respect to the Sun-Earth line) scale size of ≈450 R_E/≈70 R_E for the IMF intensity and ≈300 R_E/≳100 R_E for the logarithmic of solar wind density. Matsui et al. (2002) advanced an approach based on coherence analysis and investigated solar wind plasma and IMF variations at time scales between 16 and 512 min. They mostly found high coherence at time scales greater than ≈128 min and for spacecraft separation up to ≈44 R_E and ≈125 R_E, respectively in the direction perpendicular and parallel to the Sun-Earth line. Note that Matsui et al. (2002) reported occasional high coherence variations between 16 and 128 min, possibly related to PDS, implying that the results pertain a mixture of solar wind intervals with and without PDS. In an attempt to predict the IMF propagation delay times from L1 observation to the Earth's magnetosphere, Weimer et al. (2003) identified optimal time periods for the identification of planar front in the 7–30 min range, corresponding to 28–120 R_E. Using a combination of 24 h intervals from ACE and Wind data, Matthaeus et al. (2005) identified correlation e-folding spatial scale of ≈186 R_E for IMF fluctuations. Using similar criteria and dataset at 1 AU, Cuesta et al. (2022) reported spatial scales in the direction parallel and perpendicular to the ambient magnetic field of 310±20 R_E and 262±3 R_E for slow solar wind (<450 km s^{-1}) and 280±50 R_E and 165±8 R_E for fast solar wind (>600 km s^{-1}). Wicks et al. (2009) analyzed ≈16 h intervals from the same spacecraft pair covering separation from ≈30 R_E and ≈220 R_E. By fitting an exponential relation to the spatial correlation function of solar wind density and IMF intensity, the corresponding 95 % confidence bounds of the e-folding length scale were ≈66–86 R_E and ≈103–139 R_E during solar minimum and ≈137–245 R_E and ≈215–378 R_E during solar maximum.

There is still debate on the generation mechanisms of PDSs, but there is increasing evidence toward processes involving magnetic reconnection in the solar corona (Kepko et al. 2024). For example, Réville et al. (2020) showed in MHD simulation that periodic variations on timescales of a few hours might result from the periodic release of flux ropes from the tip of helmet streamers via a tearing mode. Additionally, PDSs are sometimes associated with small flux ropes in *in situ* measurements (Kepko et al. 2016; Di Matteo et al. 2019b; Lavraud et al. 2020). For large scale flux tubes and flux ropes, distance between IMF discontinuity or 2D reconstruction have been implemented to identified characteristic size scales (e.g., Moldwin et al. 2000; Feng et al. 2008; Borovsky 2008; Cartwright & Moldwin 2010; Yu et al. 2016; Janvier et al. 2014; Hu et al. 2018; Murphy et al. 2020; Pecora et al. 2021). Early investigations reported case studies of different types of mesoscale magnetic structures. Crooker et al. (1996) interpreted a series of quasi-periodic density enhancements (≈ 60 min) near the HCS as a bundle of flux tubes of possible solar origin flattened into sector-boundary-aligned sheets and characterized by high plasma beta and absence of a well-defined core IMF. Considering the average velocity of the solar wind (≈450 km s^{-1}) and the observed quasi-periodicity, these flux tubes showed radial length scales of ≈250 R_E. More extensive statistical analysis showed that the median diameter of a flux tube at 1 AU is ≈85 R_E (Borovsky 2008). In contrast to these observations, Moldwin et al. (2000) reported cases of isolated flux ropes with diameter of ≈270 R_E showing a cylindrical shape, low plasma beta, clear core magnetic field and IMF rotation. Statistical analysis of small flux ropes at 1 AU show radial length scales of ≈516 R_E (Yu et al. 2016) and diameter of ≈235–582 R_E (Feng et al. 2008; Cartwright & Moldwin 2010). More recently, Hu et al. (2018) defined two classes of small flux ropes with cross section scale sizes of ≈230–1200 R_E and ≈20–230 R_E with the former class manifesting properties suggestive of a closer relation to a solar source.

It follows that determination of typical size scale depends on the solar wind parcel, methodology, and criteria used to define these spatial scales. Previous comparison of PDSs observed at two spacecraft were restricted to case studies showing indications of coherent/not-coherent PDSs at azimuthal separation of 77 R_E/121 R_E (Kepko & Viall 2019) and 41 R_E/276 R_E (Villante et al. 2022). Here, we aim to statistically investigate the spatial correlation of solar wind density and IMF intensity in the context of PDSs. Note also that this is the first time that IMF intensity variations are systematically investigated during PDS intervals. In section 2, we describe the data and the methodology used. In

Section 3, we provide two case studies as examples of our target structures. Finally, in Section 4 we discuss statistical analysis results on the azimuthal properties of PDSs in the context of the mesoscale solar wind structure sizes described above and we present our conclusions in Section 5.

2. DATA AND METHODS

We use 98 s resolution solar wind density measurements from the Solar Wind Experiment instrument (SWE; Ogilvie et al. 1995) and IMF from the Magnetic Field Instrument (MFI; Lepping et al. 1995) onboard the Wind spacecraft at L1. We consider the solar wind proton (n_p) and alpha (n_α) number density; their ratio (n_α/n_p), as well as the IMF intensity ($|B|$). For the upstream solar wind parameters we also use 3 s resolution measurements of the magnetic field vector from the fluxgate magnetometer (Auster et al. 2008) and solar wind ion density (n_i) data from the Electrostatic Analyzer (ESA; McFadden et al. 2008) on board the Acceleration, Reconnection, Turbulence and Electrodynamics of the Moon's Interaction with the Sun (ARTEMIS-P1) spacecraft. The use of n_i at ARTEMIS-P1 is an inherent limitation of the data since the ESA instrument on board ARTEMIS does not discriminate between the ion populations. Note that, in slow solar wind streams, the contribution of alpha particles and/or heavier ions might influence the amplitude of the density fluctuations but not the density variations frequency and coherence level which are the focus of this work.

Table 1. Events list with frequencies of the detected periodic variations.

Start Time at ARTEMIS-P1	End Time at ARTEMIS-P1	Delay [min]	f_{Wind,n_p} [mHz]	f_{P1,n_i} [mHz]	$f_{Wind,\|B\|}$ [mHz]	$f_{P1,\|B\|}$ [mHz]
2012-01-21T16:30	2012-01-21T17:30	49.3	**0.5**	**0.6**, 2.6	0.8	0.6, 2.4
2012-01-21T20:00	2012-01-21T20:27	48.6	**0.5**, 3.3	**0.5**, 1.7	**0.5**, 2.7	**0.5**, 1.4
2012-01-22T07:00	2012-01-22T10:45	36.3	**0.7**, 1.5, 2.6, 3.5	**0.7**, 2.7, 3.6	**0.8**, 1.6, 3.0	**0.9**, 3.8
2012-01-22T17:40	2012-01-22T20:30	38.8	1.1, 2.8, 3.3	0.7, 1.8, 3.8	**1.1**, 1.4, 1.8	**0.8**, 1.8, 3.7
2012-01-24T04:32	2012-01-24T05:25	54.9	**0.5, 2.4**, 3.5	**0.5, 2.3**, 3.6	**0.7**, 3.3	**0.6**
2012-03-22T19:00	2012-03-22T20:10	44.1	**0.5**, 2.7	**0.5**, 2.3, 3.6	0.5, 1.0	2.9
2012-03-24T05:05	2012-03-24T09:00	48.3	**0.9**, 1.9, 2.6	**0.7**, 1.3	**0.8**, 1.8, 2.7	**0.8**, 2.9, 3.7
2012-04-24T01:45	2012-04-24T03:45	62.2	1.2, 3.4	1.2, 3.5	1.3, 2.8, 3.4	0.5, 1.2
2012-05-22T17:26	2012-05-22T21:41	53.1	1.4, 2.9	0.6, 1.0, 1.9, 2.9	2.0	0.6, 1.7, 2.3, 3.8
2012-11-14T04:25	2012-11-14T05:30	54.5	**0.5**, 1.5, 3.4	**0.5**, 2.8	**0.6**, 1.5, 3.1	**0.5**, 3.0
2013-06-10T02:03	2013-06-10T07:00	47.5	**0.5, 1.1**, 2.2, 2.9	**0.8, 1.1**, 2.2, 3.4	**1.2**, 1.6, 2.8, 3.3	**1.1**, 2.8
2013-07-08T00:02[a]	2013-07-08T05:02	51.5	**0.6, 1.6**	**0.6**, 0.9, **1.4**, 3.3	**0.5, 1.5**, 3.2	**0.6**, 1.0, **1.4**, 3.4
2013-07-09T06:18[b]	2013-07-09T13:30	50.6	0.7, 1.7, 2.6	0.7, 2.1	0.6, 1.8	0.6, 1.9
2013-08-04T07:00	2013-08-04T11:00	48.2	0.5, 1.6, 2.6	0.6, 1.1, 2.3	**0.5**, 1.8	**0.5**, 1.4
2014-01-01T10:30	2014-01-01T12:45	38.0	1.8	0.7, 1.5, 2.2, 3.7	0.5, 1.2	0.6, 2.4, 3.7
2014-01-01T13:38	2014-01-01T15:00	35.5	**0.7**, 2.2, 3.2	**0.7**, 1.1		0.9, 2.3
2014-05-30T12:55	2014-05-30T14:00	52.8	2.2	0.8, 3.1	1.6, 2.6	0.8, 3.1
2014-06-29T18:27	2014-06-29T21:00	46.0	0.6, 1.3	0.5, 1.7, 2.2	0.7, 1.7	0.6, 2.4
2014-07-28T04:27	2014-07-28T07:25	44.3	0.5, 1.1, 1.5	1.8, 3.3	1.6	1.8, 3.1
2014-08-26T21:41	2014-08-26T23:59	66.2	0.9	1.5, 4.0	0.8	0.6, 3.8
2014-08-27T04:40	2014-08-27T09:25	61.4	**0.6**	**0.6**, 1.3, 2.3	0.6, 1.8, 2.3	1.5, 2.4
2014-08-27T10:00	2014-08-27T12:30	61.4	0.6	0.6, 1.8	0.6, 1.5	1.6, 2.1
2015-02-16T18:30	2015-02-16T22:30	53.7	1.1, 2.6, 3.7	0.6, 1.8, 3.9	0.8, 2.7, 3.8	0.6, 1.4, 2.1, 3.8
2015-02-16T22:35	2015-02-16T23:45	53.9	**0.5, 1.3**	**0.6, 1.1**, 2.8	**0.6**, 2.9	**0.5**, 1.9, 3.0
2015-02-17T00:30	2015-02-17T02:30	52.6	0.6, 2.4	0.9	0.6, 2.3	0.7, 1.7
2015-04-20T18:45	2015-04-20T19:50	54.4	**0.5**	**0.8**, 2.8	0.5, 3.3	0.8, 2.4
2015-05-18T09:27	2015-05-18T10:45	49.8	0.7	1.2	0.7, 2.4	1.2

Table 1 *continued on next page*

Table 1 *(continued)*

Start Time at ARTEMIS-P1	End Time at ARTEMIS-P1	Delay [min]	f_{Wind,n_p} [mHz]	f_{P1,n_i} [mHz]	$f_{Wind,\|B\|}$ [mHz]	$f_{P1,\|B\|}$ [mHz]
2015-09-11T03:02	2015-09-11T06:15	45.4	**0.9, 1.4**, 3.3	**0.6, 1.7**	0.5, 1.5, 2.4, 3.1	1.0, 1.7
2015-11-13T14:15	2015-11-13T15:30	43.7	1.8, 3.4	1.3, 2.9		0.6, 1.2, 2.9, 3.9
2016-03-06T13:45	2016-03-06T17:00	57.7	0.8, 1.6, 2.9	0.7, 2.0, 3.8	**0.5**, 1.7, 3.5	**0.5**, 1.9
2016-05-08T02:15	2016-05-08T04:16	38.5	1.4, 2.3, 3.4	1.0, 2.7	**0.6**, 1.4	**0.5**, 1.1, 2.5
2016-08-03T03:06	2016-08-03T04:00	42.4	**0.6**, 2.0	**0.9**, 3.6	**0.7**, 2.0	0.8
2017-01-30T04:58	2017-01-30T12:29	45.7	0.8, 1.2, 2.7, 3.1	0.6, 2.2, 3.5	0.5, 1.1, 1.9, 2.8, 3.3	0.6, 1.5, 2.6, 3.0
2017-02-23T13:15	2017-02-23T15:04	43.8	0.8, 2.3	1.2, 2.4, 3.3	0.8, **2.1**, 2.8	**1.9**, 3.3
2017-02-27T11:45	2017-02-27T16:23	59.7	**0.7, 1.6**	**0.7, 1.6**, 2.5	**1.6**, 3.3	0.8, **1.6**, 2.4, 3.9
2017-02-28T19:30	2017-02-28T23:58	54.5	**1.6**, 2.2, 3.0	0.7, **1.5**, 2.1, 2.9	0.9, 2.2, 3.0, 3.4	0.5, 1.1, 2.2
2017-03-01T09:54	2017-03-01T12:10	47.5	0.5, 2.0, 2.9	1.2, 2.4, 2.9	**1.1, 2.3**	**1.1, 2.3**
2017-03-26T19:50	2017-03-26T21:45	57.4	0.9, 2.8, 3.8	0.9, 2.5, 3.7	**1.2**, 2.3, 4.0	**0.9**, 2.9, 3.7
2017-03-26T23:15	2017-03-27T01:45	56.7	**0.9**, 2.5, 3.2	**0.8**, 1.4	**0.5**, 2.4, 3.2	**0.6**, 1.3
2017-03-27T02:30	2017-03-27T05:30	53.7	**0.5, 1.8**, 3.5	**0.6, 2.0**, 3.3	**0.5**, 1.3, 2.6	**0.5**, 2.0, 3.3
2017-05-27T15:00	2017-05-27T19:00	47.0	0.6, 3.1	1.4	0.5, 2.2, 2.6, 3.3, 3.7	0.7, 2.1
2017-10-19T13:00	2017-10-19T14:44	46.4	2.4, 3.0, 3.7	0.9, 2.6	**2.0**, 3.1	0.8, **2.2**
2017-11-15T08:00	2017-11-15T11:30	43.5	**1.8**, 2.8	1.1, **2.1**, 3.2, 3.7	1.2, 2.2, 3.3	1.4, 2.1
2017-11-15T20:15	2017-11-15T20:55	38.5	2.2	0.9, 1.9, 3.8	0.8, 1.2, 3.2	0.8
2018-02-16T02:25	2018-02-16T03:03	54.9	2.4	1.0	2.1	1.0
2018-02-16T07:32	2018-02-16T08:31	57.0	1.1	3.5	0.8, 1.6, 2.8	0.6, 3.4
2018-05-17T00:26	2018-05-17T04:27	45.3	**0.8, 1.6**, 2.5, 3.8	**0.6, 1.7**, 3.5	1.3, 1.9, 2.4	0.8, 1.2
2018-07-11T07:04	2018-07-11T08:46	53.1	0.7, 2.4, 3.6	1.9, 3.6	0.7, 2.5, 3.9	1.9, 3.7
2018-07-11T18:01	2018-07-11T20:08	56.4	0.7, **2.7**	**2.4**, 3.6	0.7, 2.8, 3.3	1.4, 1.9, 2.8
2018-07-12T01:41	2018-07-12T06:00	48.6	1.8	2.7, 3.6	**0.6**, 1.7, 3.1	**0.7**, 2.4
2018-08-11T06:05	2018-08-11T07:45	58.7	0.5, 2.1, 3.1	0.9	**0.6**, 2.0	**0.6**, 3.2
2018-09-07T02:50	2018-09-07T04:10	62.7	**0.6**, 3.1	**0.7**	**0.5**, 1.7, 3.7	**0.6**
2018-10-07T13:43	2018-10-07T15:10	41.8	**0.6**, 2.9	**0.5**, 1.9	0.5, 1.7, 3.5	1.9
2018-10-07T15:39	2018-10-07T16:45	38.8	**0.5, 2.0**	**0.7, 2.0**	**2.0**	**2.0**
2019-07-01T03:34	2019-07-01T07:50	50.6	**0.6**, 1.9, 3.1, 3.7	**0.5**, 1.3, 3.1	**0.5**, 2.5, 3.8	**0.5**, 1.1
2019-07-03T08:50	2019-07-03T10:30	55.4	3.9	0.6, 1.9, 3.5	**0.5**, 1.9, 3.5	**0.6**
2019-07-04T17:00	2019-07-04T21:00	55.0	1.0, 2.9	0.6, 1.4	2.2, 2.9	1.3, 3.1
2019-07-30T14:07	2019-07-30T15:59	59.8	1.1, 2.7	0.7, 2.2	1.1	0.8, 2.2
2019-08-30T10:51	2019-08-30T13:20	56.1	1.1, 2.1	0.5, 1.5	0.9, 1.8	0.8, 1.4
2019-10-30T05:15	2019-10-30T07:15	41.6	**0.5**, 1.6	**0.6**, 1.2	1.4, 2.4	0.7
2019-10-30T19:50	2019-10-30T23:15	44.0	**0.9**, 1.3, 3.1	**0.9**, 2.3	**0.9**, 1.8, 2.9, 4.0	0.6, 2.4, 3.2, 3.8
2020-02-20T18:00	2020-02-20T20:30	54.8	1.5, 3.6	1.6	0.5, 2.3, 3.3	1.0, 2.1
2020-04-20T11:26	2020-04-20T12:59	44.7	1.8, 3.1	0.7, 1.4, 3.7	**0.8, 1.4**	**0.5, 1.4**, 3.9
2020-04-21T02:58	2020-04-21T05:45	45.6	**1.1**, 3.6	**1.0**, 1.5, 3.2	**1.0, 2.1**	**1.1, 2.1**
2020-05-25T04:00	2020-05-25T05:30	48.2	0.6, **1.8**, 3.2	1.0, **2.0**	**0.7**, 2.0, 3.0	**0.6**, 1.0, 3.7
2020-06-18T04:49	2020-06-18T09:30	58.9	**0.5**, 2.3, 3.4	**0.7**, 1.7, 3.9	**0.8, 1.6**, 3.4	**0.7, 1.7**
2020-06-20T00:46	2020-06-20T05:15	49.1	**1.2**, 1.7, 2.6	**1.2**, 1.7, 3.2	**1.1**, 1.6, 2.2	0.6, **1.2**, 1.8, 3.3
2020-10-15T16:30	2020-10-15T20:32	55.9	**0.5, 1.0**, 2.8	**0.8, 1.2**, 2.7, 3.7	1.4, **2.8**, 3.0, 3.9	0.8, **2.7**, 3.2

NOTE—Frequency values from the MTM spectral analysis. Bold values indicate coherent variations according to the WTC.

[a] Spacecraft separation of $|\Delta x| \approx 140.3\,R_E$, $|\Delta y| \approx 46.5\,R_E$, and $|\Delta z| \approx 7.9\,R_E$ (more details in Section 3.1).

[b] Spacecraft separation of $|\Delta x| \approx 142.0\,R_E$, $|\Delta y| \approx 56.7\,R_E$, and $|\Delta z| \approx 8.2\,R_E$ (more details in Section 3.2).

We identify PDSs in Wind and ARTEMIS-P1 time series by means of the spectral analysis procedure developed by Di Matteo et al. (2021) and based on the multitaper method (MTM; Thomson 1982). For this analysis, the plasma and magnetic field measurements at Wind are kept at the Δt=98 s cadence. The higher cadence of ARTEMIS-P1 data allows for the investigation of a wider frequency range useful for a better estimation of a power spectral density background and consequent confidence levels (Di Matteo et al. 2021). Therefore, we chose to down-sample the measurements to a Δt=60 s cadence by taking the center values of each one minute bin after applying a zero-phase forward and backward Butterworth low pass filter of order 8 and cut-off frequency 8.3 mHz. Then, we estimate the adaptive MTM power spectral density over linearly detrended three hour intervals using a time-halfbandwidth product $NW = 2.5$ and number of tapers $K = 4$ (Slepian 1978). This choice of parameters results in a Rayleigh frequency of $f_{Ray} = 1/(N\Delta t)$ ≈0.09 mHz where N_W =110 and N_A =180 are the number of data points used for the spectral analysis for the Wind and ARTEMIS-P1 spacecraft, respectively. Additionally, following Di Matteo et al. (2021), the reliable frequency range corresponds to $[2NWf_{Ray}, f_{Ny} - 2NWf_{Ray}]$ ≈0.45–4.65 mHz in which the upper limit is set by the Nyquist frequency from the Wind spacecraft ($f_{Ny} = 1/(2\Delta t)$ ≈5.1 mHz). The power spectral density is normalized by a background spectra estimated via a maximum likelihood fitting method of a bending power law model over a logarithmic binned version of the original spectrum (*bin+BPL*; see details in Di Matteo et al. 2021). Finally, we identified periodic variations in the time series at frequency values where both the normalized spectrum and an additional statistical test for phase coherence (harmonic F-test) shows enhancements above the corresponding 90% confidence threshold. The combination of the MTM and harmonic F-test is a robust approach that has been extensively tested and employed for identification of PDSs in *in situ* measurements (Viall et al. 2008; Viall et al. 2009a,b; Di Matteo et al. 2019b; Kepko et al. 2020) and remote sensing observations (Viall et al. 2010; Viall & Vourlidas 2015). Here, we implement the more recent version of this approach (SPD_MTM; Di Matteo et al. 2020) which has been employed in earlier investigations of PDSs in solar wind plasma and composition measurements (Di Matteo et al. 2022; Gershkovich et al. 2022; Gershkovich et al. 2023).

Next, we use the Cross-Wavelet Transform (XWT) and the Wavelet Coherence (WTC) following Katsavrias et al. (2021a,b). The XWT between two time-series X and Y is defined as $W_n^{XY}(f) = W_n^X(f) \cdot W_n^Y(f)^*$ where $W_n^X(f)$ and $W_n^Y(f)$ are the corresponding wavelet spectra. The XWT examines the relationship in the time-frequency space between two time series and identifies regions of high common power and consistent phase relationship. For such regions, the WTC closely resembles a localized correlation coefficient in time–frequency space and varies between 0 and 1, corresponding to non-coherent and coherent periodic behavior, respectively (Katsavrias et al. 2016, 2022). Note that for this analysis the time series are reduced to the same cadence and similar results are obtained by either using Δt=98 s or Δt=60 s. The statistical significance level of the WTC is estimated using Monte Carlo methods. In detail, we generate a large ensemble of first order auto-regressive surrogate data set pairs with the model coefficient estimated from the input datasets (see also Grinsted et al. 2004). For each synthetic time series pair, we calculate the WTC values obtaining a distribution from which we define a significance level for each frequency. Particularly, we classify as high coherence events the periodic variations at the two spacecraft for which the WTC remains consistently above 0.7 for more than two times the corresponding period. Periodic variations for which this condition is not satisfied or the WTC is consistently below 0.7 are classified as low/no coherence events.

3. EVENTS SELECTION CRITERIA AND EXAMPLES

We focus on PDSs observed in high density, slow solar wind streams. Even though in these conditions we are selecting a particular subset of all the PDSs, these structures create large variations in density/dynamic pressure, making them easier to identify, and are more likely to trigger relevant space weather phenomena. Using 9 years (2012–2020) of solar wind observations from the ARTEMIS-P1 satellite, we searched for time intervals satisfying the following criteria: (i) ARTEMIS-P1 satellite located upstream of the dayside magnetosphere ($9 \leq$ MLT ≤ 15); (ii) solar wind density increases from relatively steady conditions toward maximum values above 15 cm^{-3} for at least 1 hour; (iii) solar wind speed $V_{SW} \leq 450\,\mathrm{km\,s}^{-1}$ throughout the entire event. Note that the last two criteria tend to be satisfied in small compression regions. We further exclude time intervals: (i) with a sharp increase in density associated with shocks which could affect the results of the spectral analysis; (ii) when ARTEMIS-P1 is in the moon's plasma wake; (iii) when there are no simultaneous availability of solar wind observations from the Wind spacecraft. We examined each interval visually to define the entire duration of the density increase, and not only the part which was above 15 cm^{-3}.

To allow reliable and uniform results for the spectral analysis, we analyze observations on three hour running windows centered along the identified time intervals. Finally, we impose a maximum 10% of missing data with gaps of no more than four consecutive points. These criteria resulted in 68 events all accompanied by PDSs at frequencies within the 0.4–4.0 mHz range, while there was no event without PDSs in both spacecraft. A summary of time interval, delay, and selected frequency is available in Table 1. In what follows we present two examples in which there was high or low/no coherence between PDSs with similar frequency detected at Wind and ARTEMIS-P1.

3.1. *A high-coherence example: The 2013 July 8 event*

On 2013 July 8, the Wind and ARTEMIS-P1 spacecraft were located at X_{GSE} ≈204.9 R_E, Y_{GSE} ≈50.3 R_E, Z_{GSE} ≈−12.6 R_E and X_{GSE} ≈64.6 R_E, Y_{GSE} ≈3.8 R_E, Z_{GSE} ≈−4.7 R_E, roughly between 00:00–05:00 UT (Figure 1g–1h). We shifted the Wind observations by a time lag of ≈51.5 min estimated using the average spacecraft locations and solar wind speed along the X_{GSE} direction at ARTEMIS-P1 (≈288.7 km s^{-1}). During the 00:35–03:55 UT sub-interval, the two spacecraft observed a solar wind stream of almost constant velocity at ≈300 km s^{-1} (Figure 1a), characterized by an overall increase of solar wind density from ≈9.0 cm^{-3} to maximum values of ≈14.5 cm^{-3} at Wind (Figure 1c) and from ≈10.4 cm^{-3} to ≈16.6 cm^{-3} at ARTEMIS-P1 (Figure 1d). Both solar wind density and IMF intensity showed a clear periodic behavior at both Wind and ARTEMIS-P1 (Figures 1c–1f). The time series anti-correlation together with the analysis of the thermal (protons and alphas), magnetic, and total pressure at Wind (not shown) indicate that the PDSs were in pressure balance conditions showing plasma $\beta \gtrsim 1$. A periodic behavior was also observed in the n_α/n_p ratio (Figure 1b), only available from Wind observations, with higher amplitudes during the high density interval of interest, before a sudden drop to an almost constant value of 0.012 in correspondence to the solar wind velocity increase. These properties are consistent with previous reports of PDSs (Kepko et al. 2016; Di Matteo et al. 2019a; Kepko et al. 2020; Di Matteo et al. 2022; Gershkovich et al. 2022). We then applied the SPD_MTM spectral analysis procedure (see Section 2) to investigate the periodic nature of the solar wind density and IMF intensity. The results, available in Table 1, show three shared frequency bands at 0.5–0.6, 1.4–1.6, and 3.2–3.4 mHz at both spacecraft with an additional component at 0.9–1.0 mHz only present in the ARTEMIS-P1 observations.

Figure 2 shows the XWT (middle column) and WTC (right column) calculations used to study the interrelation between the periodic behavior of Wind and ARTEMIS-P1 solar wind density (top row) and IMF intensity (bottom row) measurements. Arrows indicate the phase relationship between the two time series in the time–frequency space. For the WTC, the regions covered by arrows correspond to portions with high confidence level ≥0.7. The left column panels

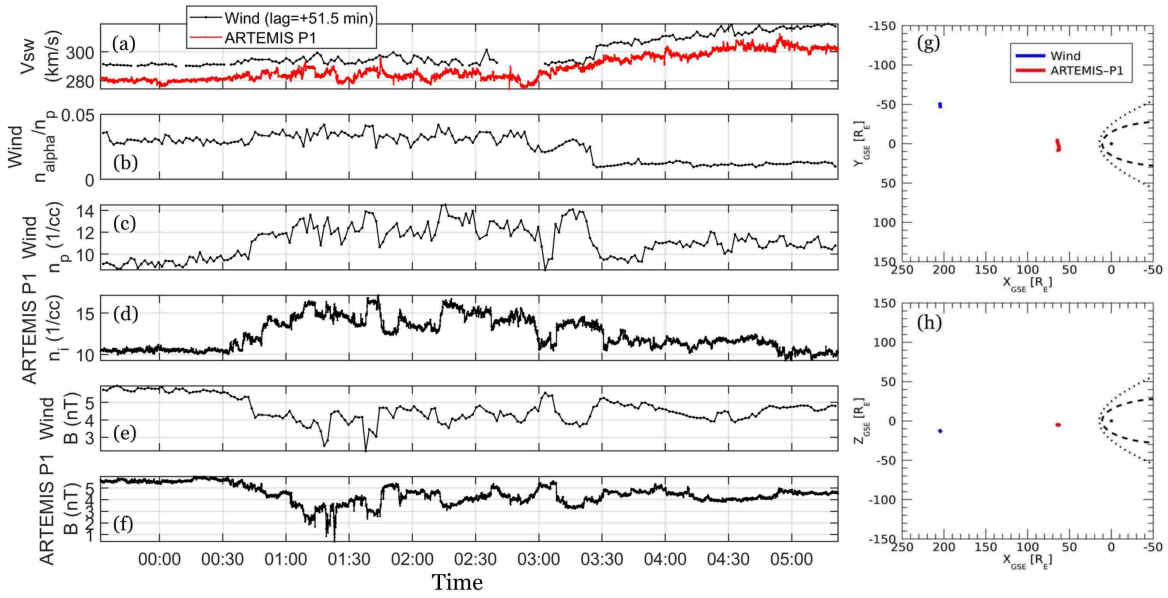

Figure 1. Overview of the 2013 July 8 event. (a) Solar wind speed at Wind (black line) and ARTEMIS-P1 (red line). (b) n_α/n_p ratio from Wind. (c-d) Proton and ion density from Wind and ARTEMIS-P1, respectively. (e-f) IMF from Wind and ARTEMIS-P1, respectively. Wind is shifted with 51.5 minutes time-lag. (g-h) Location of Wind (blue points) and ARTEMIS-P1 (red points) in GSE coordinates.

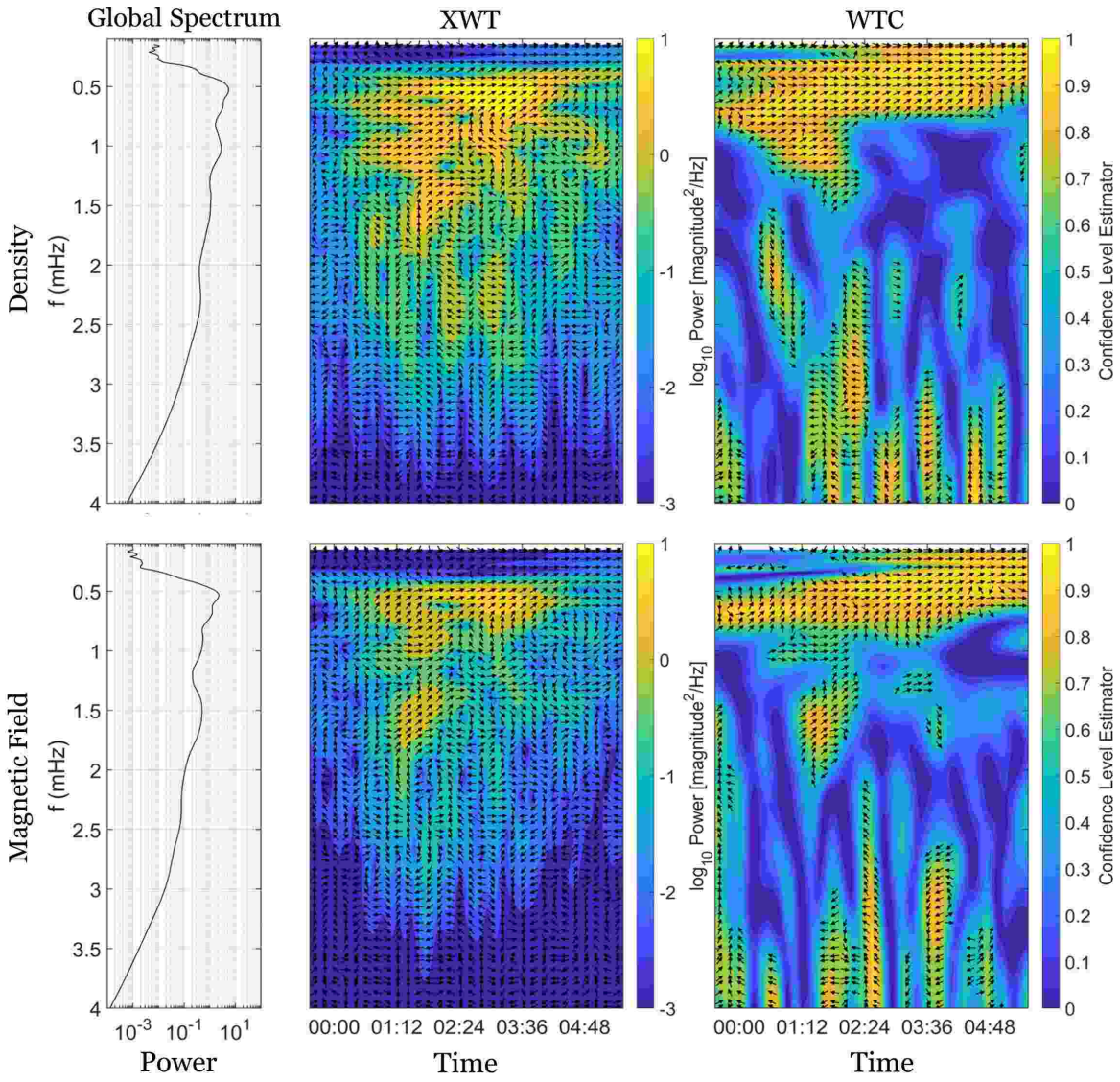

Figure 2. Global wavelet (left panels), XWT (middle panels) and WTC (right panels) between Wind and ARTEMIS-P1 observations of solar wind density (top panels) and IMF intensity (bottom panels). Arrows indicate the phase relationship between the two time series in the time–frequency space. Those pointing to the right correspond to an in-phase behavior, while those to the left an anti-phase behavior. The downwards pointing arrows indicate 90^o lead of the first data series (in our case Wind time-series). The area covered by arrows in the WTC panels manifest confidence level $\geq$0.7.

depict the time average of the XWT spectrum, namely the global spectrum, showing clear enhancements centered at frequencies similar to the ones reported in Table 1: $\approx$0.5 , $\approx$1.0 , and $\approx$1.5 mHz. The most pronounced feature is the $\approx$0.5 mHz periodicity in both solar wind density and IMF intensity, which exhibited high common power and in-phase relationship with very high coherence (R>0.9) during the entire event duration. Similar behavior is exhibited by the variations at $\approx$1.0 mHz and at $\approx$1.5 mHz showing higher and more persistence coherence in density and in IMF intensity, respectively. Finally, higher frequencies (3.2–3.4 mHz) exhibit no common power and very low coherence. These results suggest that the same train of lower frequency PDSs transited at the two spacecraft locations.

3.2. *A low-coherence example: The 2013 July 9 event*

On 2013 July 9, the Wind and ARTEMIS-P1 spacecraft were located at X_{GSE} $\approx$204.6 R_E, Y_{GSE} $\approx$46.0 R_E, Z_{GSE} $\approx-$13.3 R_E and X_{GSE} $\approx$62.5 R_E, Y_{GSE} $\approx-$10.7 R_E, Z_{GSE} $\approx-$5.1 R_E, roughly between 06:20–13:30 UT (Figure 3g–3h). Similar to the previous event, we shifted the Wind observations by a time lag of $\approx$50.6 min estimated using the average spacecraft locations and solar wind speed along the X_{GSE} direction at ARTEMIS-P1 ($\approx$297.7 km s^{-1}).

Between 10:00 UT and 13:45 UT, a gradual density (Figure 3c–3d), velocity (Figure 3a), and IMF intensity (Figure 3e–3f) increase was detected at both ARTEMIS-P1 and time-shifted Wind measurements. However, the observed variations have some distinct differences at the two spacecraft locations. For example, the ramp in solar wind density and IMF intensity, starting at about 10:00 UT, is smoother for Wind observations and it is associated with a short density enhancement only at ARTEMIS-P1. There was no evident anti-correlation between solar wind density and IMF observations at Wind. Consistently, pressure balance conditions were absent during this interval showing plasma $\beta < 1$. Finally, the n_α/n_p ratio remained at values of 0.02–0.03 showing only signs of additional higher frequency variations toward the end of the time interval. Applying the SPD_MTM procedure to the spacecraft observations, we identified two shared frequency bands at ≈0.6–0.7 and ≈1.7–2.1 mHz (Table 1). An additional periodic fluctuation at ≈2.6 mHz occurred in Wind density observations toward the end of the time interval concomitant with the higher frequency variations detected in the n_α/n_p ratio. Despite the similarity with the previous event in terms of spatial separation and identified periodicity, the solar wind properties lacked characteristics typically associated with PDSs.

The different behavior between Wind and ARTEMIS-P1 observations is also depicted in the XWT and WTC results (Figure 4). A pronounced common power appeared only at ≈0.7 mHz with coherence levels way below the 0.7 threshold we imposed, spanning WTC values of 0.2–0.5. Higher frequencies exhibited both low power and low coherence. Possible explanations for the similarities in the observed frequencies and the lack of coherence could be that one or both spacecraft observed the PDS edges or that these structures have lower amplitude variations which might be more affected by processes en route leading to lower coherence levels (Dalin et al. 2002).

4. STATISTICAL RESULTS

We repeated the analysis for 68 PDS events and investigated the results in terms of frequency distribution, coherence, and spacecraft locations. Figure 5 shows the distribution of the frequency associated with periodic variations in solar wind density (Panel a–b) and IMF intensity (Panel c–d) for Wind and ARTEMIS-P1. We considered the periodic variations at the two spacecraft to be comparable if their frequency separation is smaller than the spectral window half-bandwidth ($\approx 3f_{Ray}$ ≈0.3 mHz). We organized the frequency distribution in bins of the same width. All of the distributions manifested the highest occurrence of events at ≈0.5–0.8 mHz. Additional local enhancements appeared centered at ≈1.9 mHz, more evident in the Wind observations for both parameters, and with more variability within ≈2.7–2.9 mHz and ≈3.2–3.8 mHz. Considering the level of coherence between the variations, we obtained three categories: (a) similar frequency ($|f_W - f_A| < 3f_{Ray}$) with high coherence; (b) similar frequency with low/no coherence;

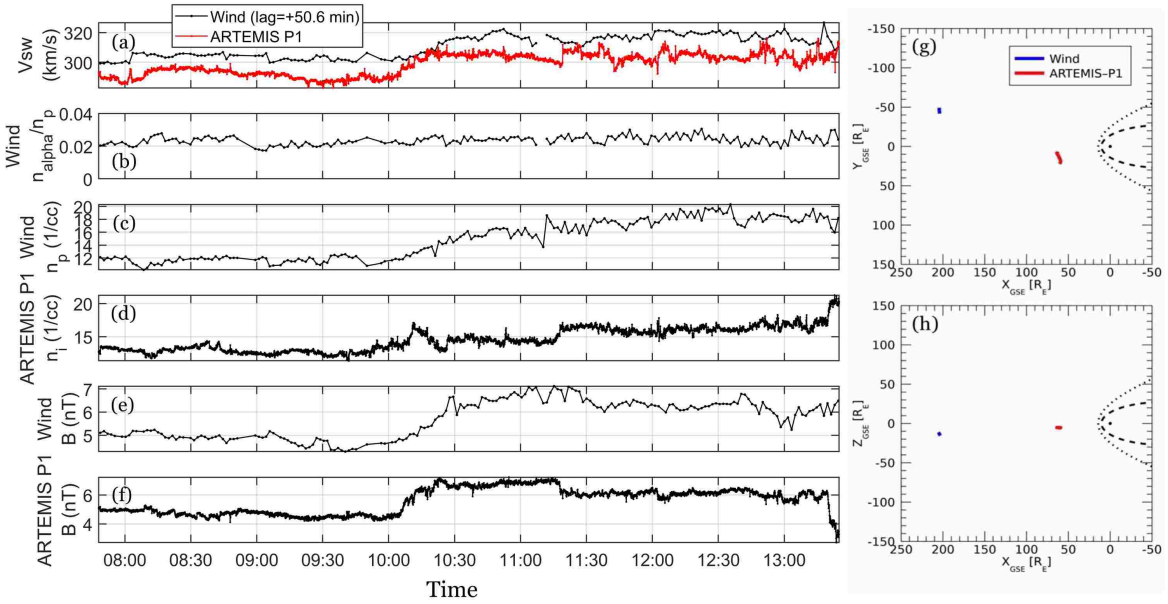

Figure 3. Same as figure 1 for the July 9, 2013 event. (a) Solar wind speed at Wind (black line) and ARTEMIS-P1 (red line). (b) n_α/n_p ratio from Wind. (c-d) Proton and ion density from Wind and ARTEMIS-P1, respectively. (e-f) IMF from Wind and ARTEMIS-P1, respectively. Wind is shifted with 50.6 minutes time-lag. (g-h) Location of Wind (blue points) and ARTEMIS-P1 (red points) in GSE coordinates.

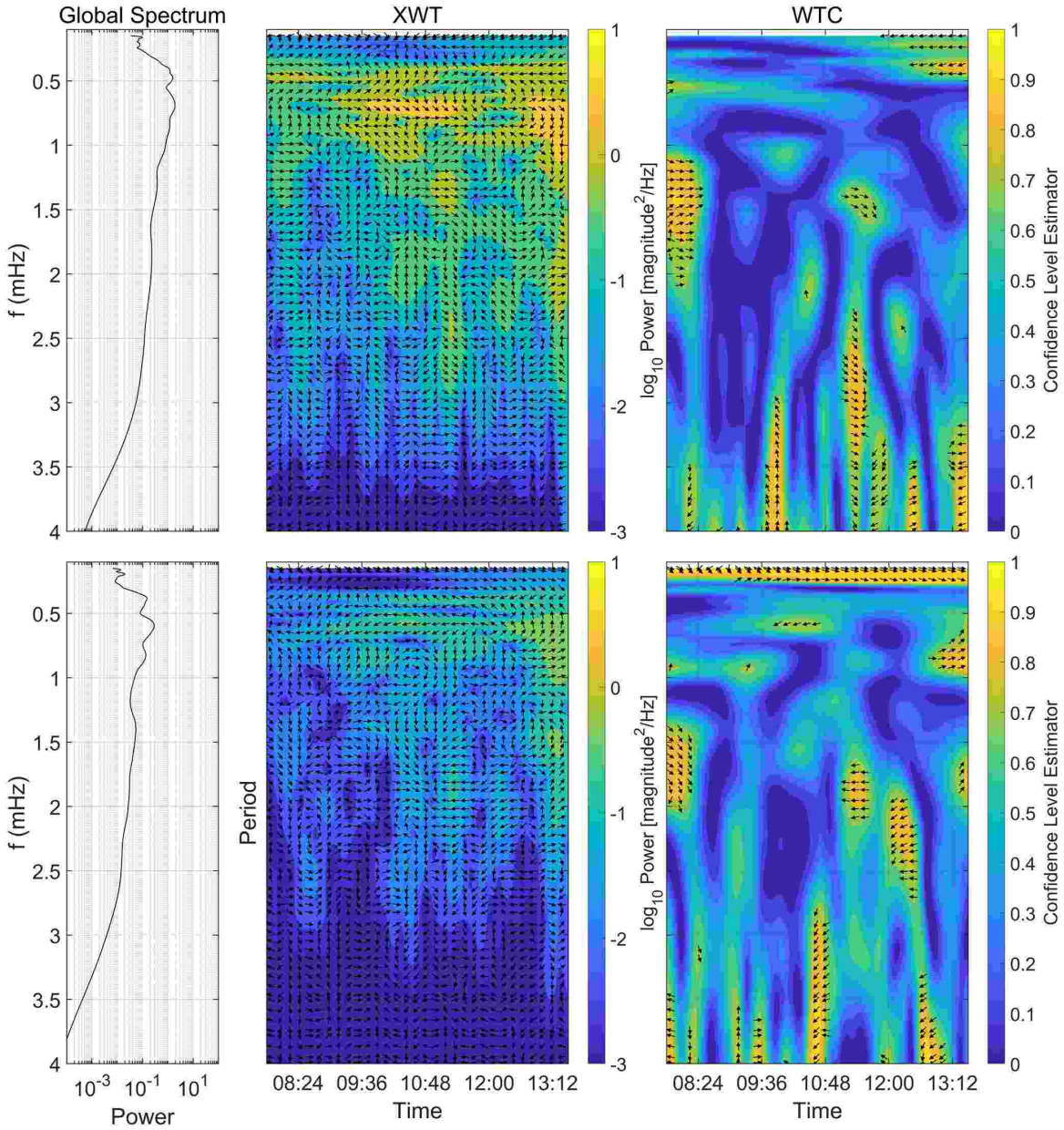

Figure 4. Same as figure 2 for the July 9, 2013 event.

and (c) different frequency ($|f_W - f_A| > 3f_{Ray}$). As shown in Figure 5, the occurrence of PDSs with high coherence at similar frequency (blue bars) is higher at low frequencies ($f \leq$1.0 mHz) and progressively decreases until frequency values of ≈2.8 mHz. PDSs with low or no coherence (magenta bars) show a similar behavior but with frequency up to ≈4.0 mHz and two small enhancements at ≈2.7–2.9 mHz and ≈3.5–3.8 mHz. This set of discrete frequencies, that is ≈0.5–0.8, ≈1.9, ≈2.7–2.9, and ≈3.2–3.8 mHz is comparable to the ones previously reported in solar wind density observations (Viall et al. 2009a; Di Matteo & Villante 2017, and references therein). Results for IMF intensity manifest similar frequency distributions with more variability above ≈3.0 mHz.

Due to the clustering of events at preferential frequencies, we divided our dataset into three groups: (a) 0.4$\leq f <$1.0 mHz; (b) 1.0$\leq f <$2.5 mHz, (c) 2.5$\leq f <$4.0 mHz. Considering the solar wind speed at each event, these groups are equivalent to radial length scales of: (a) 49$< L_x <$160 R_E; (b) 20$< L_x <$68 R_E, and (c) 10$< L_x <$30 R_E. Figure 6 shows scatter plots of the events based on the spacecraft separation along the GSE directions. Blue triangles and magenta circles correspond to intervals with PDSs at similar frequencies showing high and low/no coherence,

respectively; black stars indicate cases of PDSs at different frequencies. The bar plots show, with the same colors, the corresponding occurrence rates with bin width defined to obtain a uniform number of at least 15 events in each bin. Given the low number of events, the major source of uncertainty is due to the choice of the bin width which results in a quantization effect, that is the variations of the occurrence rate of each category that we would obtain by simply adding or removing an event of the same category (black lines in Figure 6). Note that we repeated the analysis using four uniform bins and obtained similar results. For PDSs with periodicities lower than ≈1.0 mHz (Figure 6a), the occurrence rate of events with high coherence and similar frequency remains at almost constant values along $|\Delta x|$ and $|\Delta y|$ (≈41–47 %). Instead, a dip of ≈20 % appears for $|\Delta z|$ separation at ≈5.5–11 R_E. In the 1.0–2.5 mHz range (Figure 6b), occurrence rates of events at similar frequencies (blue plus magenta) decrease from ≈36 % to ≈22 % with increasing $|\Delta y|$, increase with increasing $|\Delta x|$, and decrease with decreasing $|\Delta z|$. However, spacecraft separations at larger $|\Delta x|$ and smaller $|\Delta z|$ correspond to small and large $|\Delta y|$, respectively, suggesting that the separation along the Y_{GSE} component is mainly regulating the distributions. These relations are even more pronounced for PDSs at frequencies above 2.5 mHz (not shown). However, these PDSs correspond to periods of 4.0–6.5 min which are comparable to the uncertainties in the estimation of the time-lag between the time-series of the two spacecraft, which might also explain the low occurrence of high coherence events (Figure 5). For events identified in the IMF intensity (Figure 7), we obtained occurrence rates with similar trends but different magnitude. At frequencies lower than 1.0 mHz, we observed almost constant values for high coherence events for $|\Delta y|$ (≈31–39 %) and $|\Delta z|$ (≈30–40 %), while occurrence rates decrease from ≈47 % to ≈29 % with increasing $|\Delta x|$. At frequencies between 1.0 and 2.5 mHz, we obtained uniform rates of high coherence events along all directions (≈12–17 % for $|\Delta x|$, ≈11–21 % for $|\Delta y|$, ≈11–18 % for $|\Delta z|$) as well as for low/no coherence events (≈15–25 % for $|\Delta x|$ and ≈18–22 % for $|\Delta z|$), except for $|\Delta y|$ showing a sharp drop at larger separations from ≈28 % to ≈4 %. At frequencies of ≈2.5–4.0 mHz (not shown), we observed differences

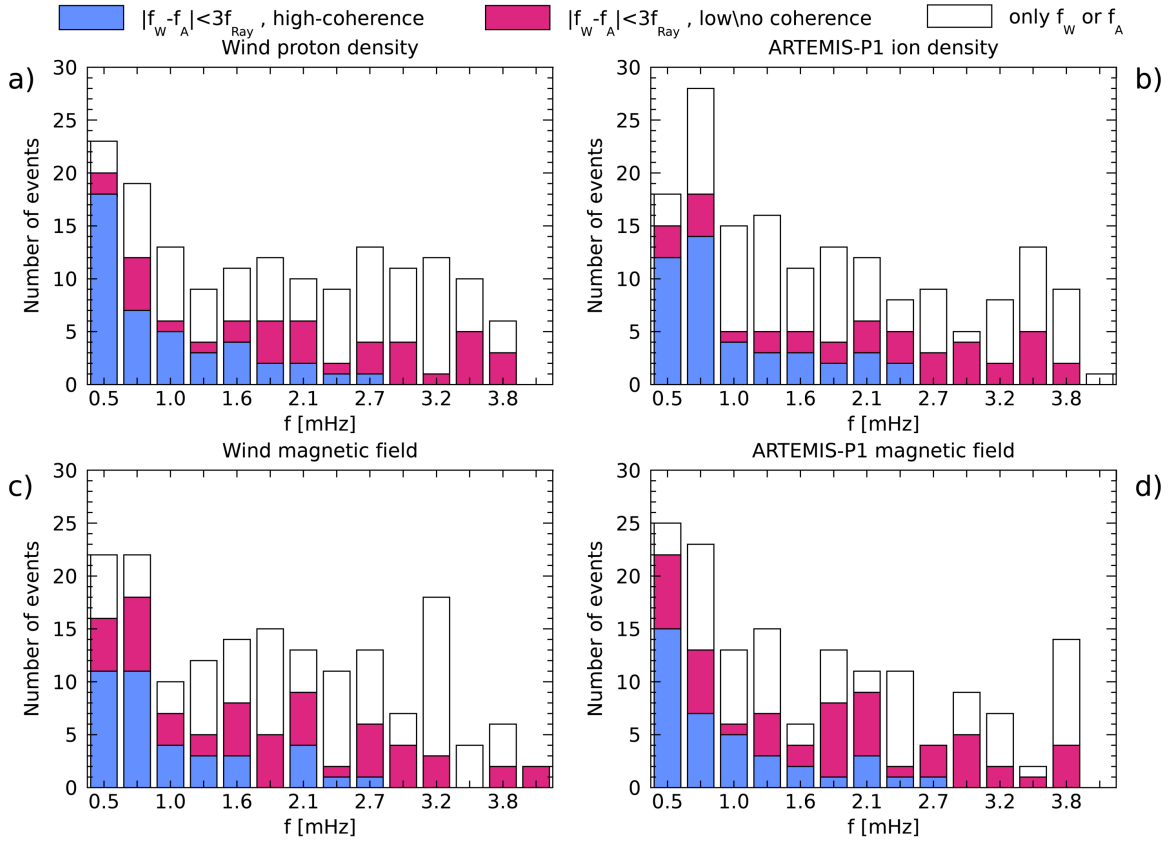

Figure 5. Distribution of frequencies identified in solar wind density and IMF intensity observations at Wind (panel a and c) and ARTEMIS-P1 (panel b and d). The colors identify subgroups of the distribution in which the difference in frequency observed by the two spacecraft is lower than $3f_{Ray}$ for structures showing high-coherence (blue) and low/no coherence (magenta).

with occurrence rate trends from the solar wind density and again a low number of high coherence events which further suggest the relevant role of time-lag uncertainties.

5. DISCUSSION

We investigated the properties of PDSs identified in 68 intervals of high density, slow solar wind stream at Wind and ARTEMIS-P1. Through the analysis of solar wind density, we identified 158 and 166 periodicities at Wind and ARTEMIS-P1, respectively. Among them, 79 cases showed similar frequencies, while 43 cases exhibited high-coherence. High coherence variations at frequencies above ≈1.0 mHz occurred in association with high coherence variations at lower frequencies in 10 out of 16. For IMF intensity measurements, we identified 169 and 153 periodicities at Wind and ARTEMIS-P1, respectively. Among them, 87 cases showed similar frequencies, while 38 cases also exhibited high-coherence. High coherence variations at frequencies above ≈1.0 mHz occurred in association with high coherence variations at lower frequencies in 5 out of 14 cases. During interval of PDSs, the pressure balance conditions is one of their occasional properties (e. g., Di Matteo et al. 2019b). However, at 1 AU, the plasma beta is generally around 1, so the kinetic pressure and magnetic pressure are comparable. Additionally, slow solar wind shows high density but low temperature, suggesting the kinetic pressure should not change significantly, so the variations of IMF intensity should be limited. However, our spectral analysis approach can reveal the occurrence of periodicity in a time series even though their amplitude is limited (Di Matteo & Villante 2017). Note that this is the first time that IMF intensity variations associated with PDSs have been statistically investigated. For IMF observations, we found this correspondence in 98 out of 169 cases at Wind and in 110 out of 153 cases at ARTEMIS-P1.

Results from multi-spacecraft studies showed that solar wind parcels manifest a weak but significant dependence on separations perpendicular to the Sun-Earth line (Dalin et al. 2002). Additionally, recent investigations provided supporting evidence of the preferential azimuthal extension of solar wind parcels. Burkholder et al. (2020) used a

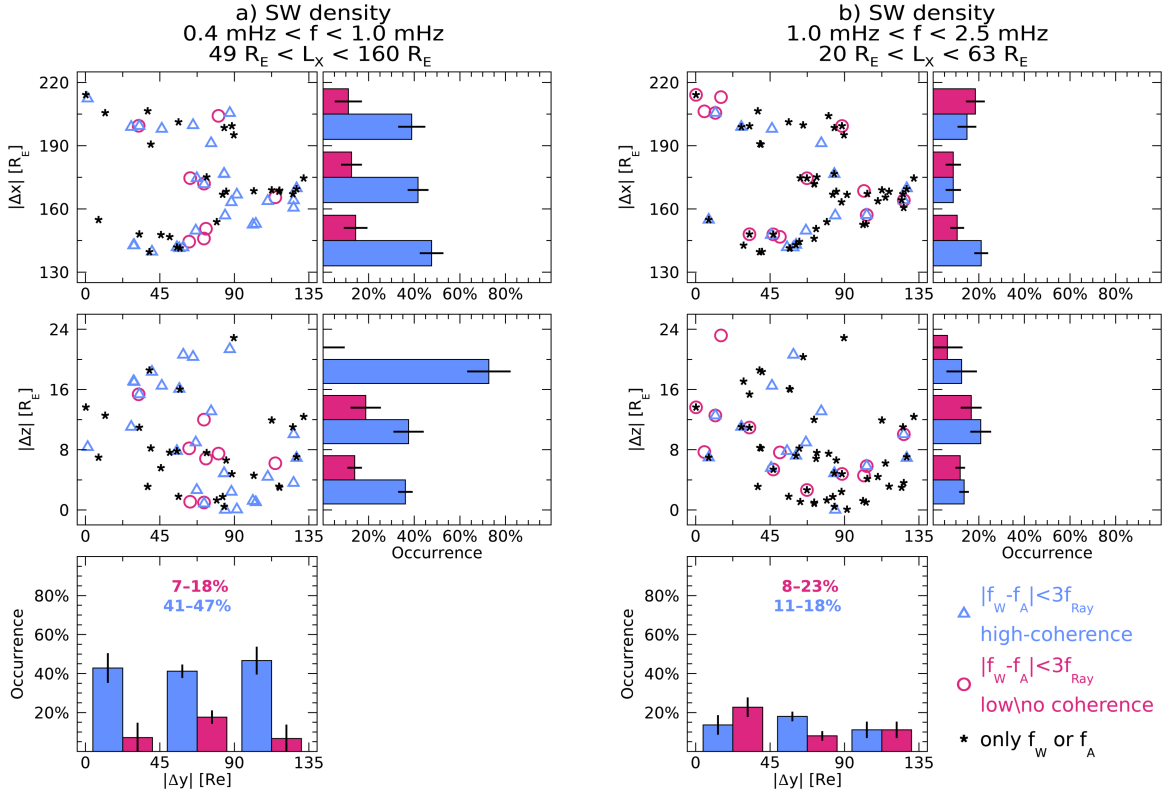

Figure 6. Scatter plots and occurrence rate distributions as a function of the $|\Delta X_{GSE}|$, $|\Delta Y_{GSE}|$, and $|\Delta Z_{GSE}|$ separation between Wind and ARTEMIS-P1 for PDSs at frequencies of $0.4< f <1.0$ mHz (panel a) and $1.0< f <2.5$ mHz (panel b). Colors and symbols indicate intervals manifesting PDSs at different frequency (black stars) and at similar frequency with high (blue triangles) or low/no (magenta circles) coherence. Black lines in the occurrence distribution indicate the uncertainty related to the quantization effect due to the low number of events. Percentages in the bottom panel indicate the range of the observed occurrence rates for $|\Delta Y_{GSE}|$ spacecraft separation.

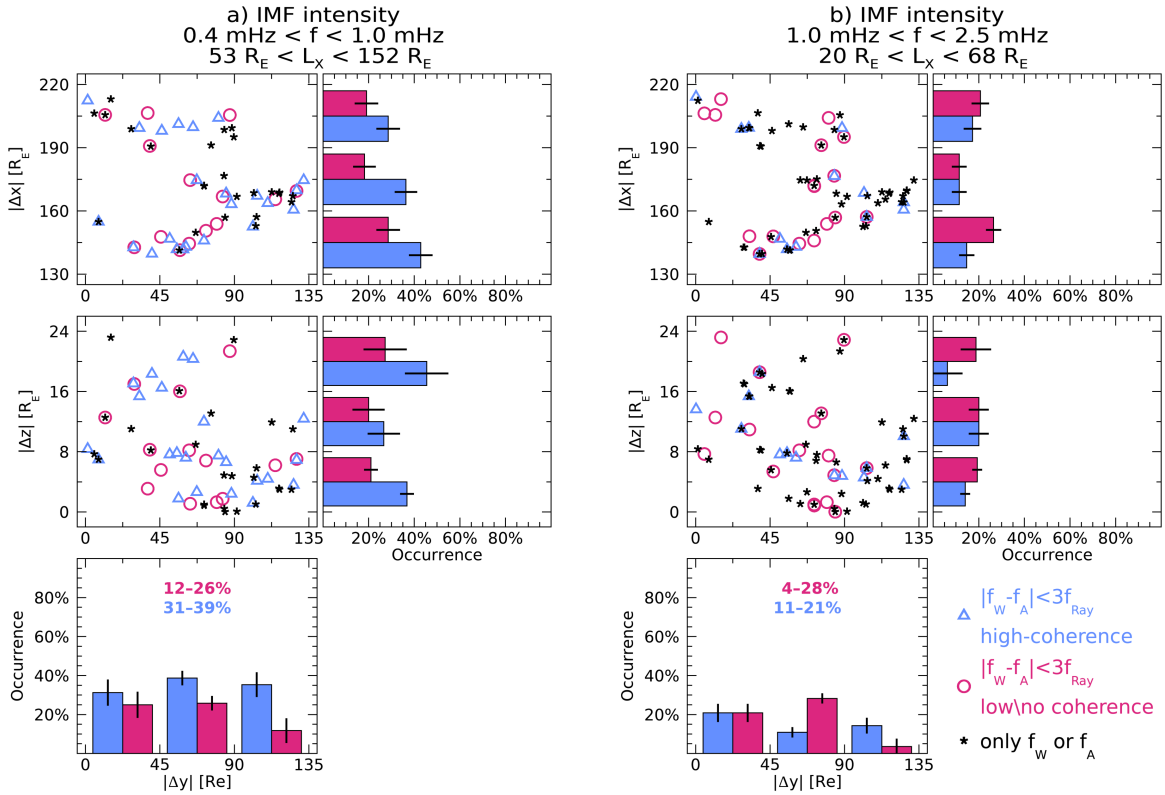

Figure 7. Same as Figure 6 but for periodic variations identified in IMF intensity observations.

novel multi spacecraft approach able to resolve solar wind spatial gradients on scale sizes of the order of the Earth's magnetosphere dimensions. While they found significant structures in both the X_{GSE} and Y_{GSE} direction, their spatial reconstructions revealed solar wind parcels elongated along the Y_{GSE} direction up to scale size of the order of the spacecraft separation. In a very recent investigation using 10 years of in situ data from the ACE mission, Wang et al. (2024) found that the density correlation scale in directions quasi-parallel to the mean magnetic field is slightly larger than the one in quasi-perpendicular directions. This translates to slightly larger dimensions along the direction perpendicular to the Sun-Earth line at 1 AU given the average orientation of the interplanetary magnetic field. These studies don't distinguish between different solar wind structures, that is CIRs, CMEs, and PDSs among others. A recent study using STEREO-A and Wind in situ measurements showed that magnetic ejecta, even though at bigger scale sizes, are elongated in the direction perpendicular to the Sun-Earth line by a factor ≈ 2 (Lugaz et al. 2024). In interpreting the trend in our occurrence rate distribution, the separation along the Z_{GSE} component is unlikely to play a role due to the relatively small values. Along the X_{GSE} direction, possible sources of change in coherence are: (i) dynamical evolution of the solar wind parcel (time evolution); (ii) contribution of aberration effect (spatial effect). For the former, we don't expect the solar wind to evolve significantly between the Wind and ARTEMIS-P1 location since the coherent/not-coherent classification pertains to intervals with the same periodicity in density and/or magnetic field at the two spacecraft locations. This means that the spatial extent of the PDSs along the X_{GSE} direction is not changing significantly. In fact, we use the period of these variations to determine the radial extent of PDSs. For the aberration effect, the coherence might be affected since we could observe different parts of a solar wind parcel even when the two spacecraft are aligned. From observations at L1 to the bow-shock, the cumulative effect of aberrations amounts to tens of R_E (Borovsky 2022), that is an order of magnitude smaller than most of the scale sizes in the direction perpendicular to the Sun-Earth line reported in the literature. This further supports our hypothesis, that the results should mostly depend on the azimuthal separation of the two spacecraft. This assumption is supported by our observations showing spacecraft separation along the azimuthal direction often regulating the occurrence rate distribution along the other directions. The almost constant rate of PDSs at similar frequencies, either with high or low coherence, indicates that the azimuthal scale of the PDSs is at least as large as the maximum separation of the two spacecraft, that is $\Delta y \approx 130\,R_E$ for the PDS groups at $49 < L_x < 160\,R_E$ and $20 < L_x < 68\,R_E$. Additionally, the

higher number of high coherence events for PDSs with larger L_x suggests that the actual PDS azimuthal scale might be regulating the occurrence rates.

To test this hypothesis, we define a simple forward model represented in Figure 8a. Since the azimuthal spacecraft separation appears to regulate the occurrence distributions along the other two orthogonal directions, we only use the Y_{GSE} coordinate as a free parameter. The purple and yellow regions represent two PDSs belonging to the same PDS group as defined above. As a PDS propagates toward Earth, two spacecraft, represented by connected circles (Wind) and diamonds (ARTEMIS-P1), would observe a similar periodicity with high coherence when they are within a PDS core region (L_C), represented by the darker regions. The lighter areas (PDS tails/ambient solar wind), with characteristic scale L_T, correspond to the region at the boundary of the PDS, in which we hypothesize that the amplitude of the variations starts to decrease (low-coherence) until eventually it disappears outside the PDS (no-coherence). When both spacecraft are within this region, or respectively in the PDS core and tail, we would observe similar periodicity with low/no coherence. Finally, if two different PDSs go past each spacecraft, we would observe different periodicity. Since our event list comprises time intervals in which PDSs are always detected, we simplify the simulation setup by allowing no gap between adjacent PDSs. Consequently, the resultant PDS scale along the Y_{GSE} direction is $L_y = L_C + 2L_T$. We define a Y_{GSE} array domain, limited by the spacecraft extreme azimuthal locations during our 68 intervals ($Y_{min} \approx -103\,R_E$ and $Y_{max} \approx 102\,R_E$), with a cadence corresponding to a third of the minimum spacecraft separation ($|\Delta y| \approx 2\,R_E$). By projecting the actual locations of Wind and ARTEMIS-P1 on such domain we obtain the occurrence rates of the three categories of events. We explored $20 \leq L_C \leq 500\,R_E$ and $2 \leq L_T \leq 100\,R_E$, both with a $2\,R_E$ step. For each combination, we repeated the simulation 10,000 times using uniform random numbers across the domain to define the position of PDSs. The results in Figure 8b shows the occurrence rates for high and low/no coherence events as a function of L_C and L_T in blue and magenta color scale contours, respectively. Finally, we marked with striped yellow and purple areas, the range of occurrence rates observed as a function of $|\Delta y|$ separations for solar wind density and IMF intensity. The resultant L_C and L_T are reported in Table 2 together with the overall effective scale along the Y_{GSE} direction (L_y). For smaller PDSs, the azimuthal scale inferred from solar wind density and IMF intensity completely overlaps in the L_C and L_T space, yielding an azimuthal scale of $\approx$187–198 R_E. This

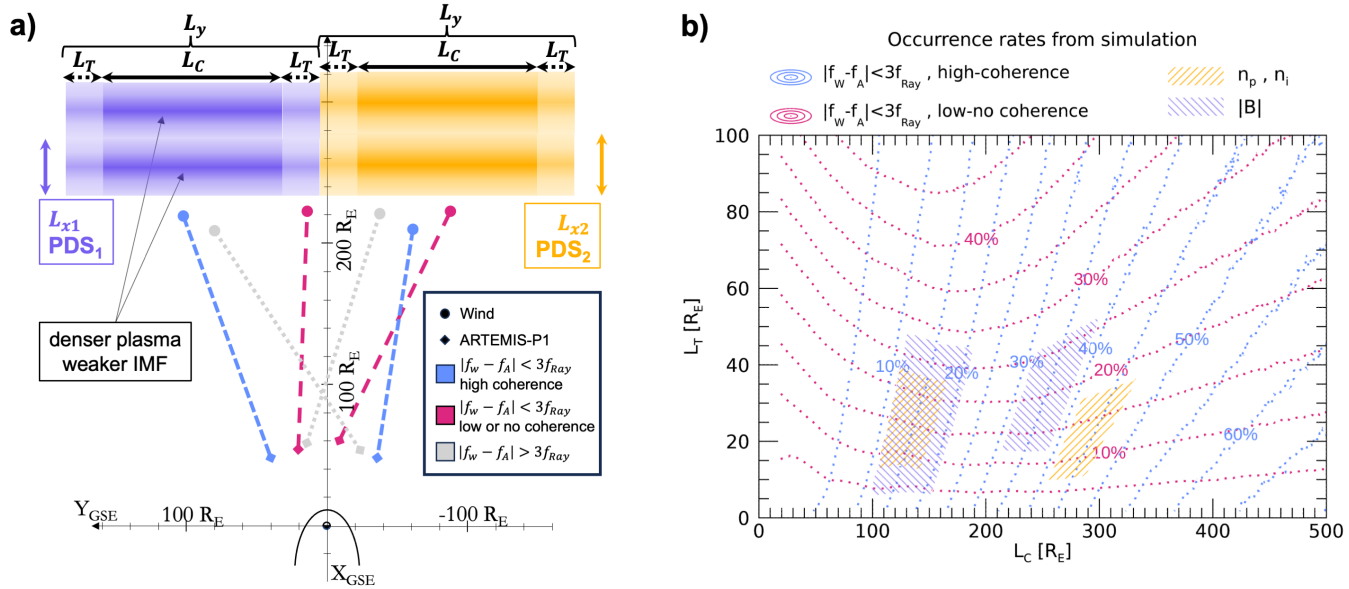

Figure 8. Panel a, schematic representation to scale of the simulation setup depicting the transit of PDSs. Purple and yellow stripes represent structures at different frequency/radial length scale. The dark and light areas indicate the high and low/no coherence regions of azimuthal scale L_C and L_T, respectively. Connected circles and diamonds show possible spatial configuration of Wind and ARTEMIS-P1. Colors indicate the corresponding expected outcome of the spectral plus coherence analysis, namely different PDSs (grey) and same PDSs with high (blue) or low/no (magenta) coherence. Panel b, occurrence rate contour levels for PDSs with high (blue) or low/no (magenta) coherence obtained by 10,000 simulations of PDS transit at the actual spacecraft position for each combination of L_C and L_T. Striped yellow and purple areas cover the occurrence rates observed in solar wind density and IMF intensity as a function of the $|\Delta y|$ spacecraft separations for the two larger PDS groups from Figure 6a–b and Figure 7a–b.

scale is slightly larger than the maximum $|\Delta y|$ spacecraft separation in our dataset ($\approx$130 R_E). This is in agreement with the observed decrease of the number of similar frequency events with $|\Delta y|$ shown in Figure 6b and Figure 7b suggesting that the maximum spacecraft separation is close to the azimuthal scale of smaller PDSs. For larger PDSs, even though the solar wind density inferred L_C and L_T is larger and smaller, respectively, than the ones estimated from the IMF intensity, there is overlap in estimates of the L_y scale ($\approx$326–340 R_E). This indicates that for PDSs at larger radial length scales, the spatial correlation along the Y_{GSE} direction falls off more rapidly for the IMF intensity than for the solar wind density, which might be a specific property of this PDS group.

The estimates of the PDS scales perpendicular to the Sun-Earth line are at least two times larger than the typical scale values obtained from previous correlation or coherence analysis (Chang & Nishida 1973; Crooker et al. 1982; Collier et al. 2000; Richardson & Paularena 2001; Matsui et al. 2002; Weimer et al. 2003), except for the correlation length reported by Matthaeus et al. (2005) and Cuesta et al. (2022) for IMF fluctuations showing similarities with our small PDSs. Both small and large PDS azimuthal scales are instead consistent with correlation scales of structures of possible solar origin reported by Wicks et al. (2009). Interestingly, our example of a high-coherence event shows clear n_α/n_p periodicities supporting the PDSs solar origin, while the low-coherence example showed little n_α/n_p variations consistent with formation either at the Sun or en route. A recent statistical investigation demonstrated how the alpha-to-proton ratio, even though not as good as heavy ions, is a reasonable asset in support of the solar origin of solar wind parcel when associated with PDSs (Kepko et al. 2024). Wicks et al. (2009) also reported that high correlation azimuthal scales for solar wind density variations were of the same order or smaller than the ones in IMF intensity, in contrast with our results. However, a direct comparison might be misleading since Wicks et al. (2009) investigated correlations only in function of the absolute spacecraft separation.

Typical scale of magnetic flux tubes and/or flux ropes refers to their diameter, hence corresponding to either radial or azimuthal direction in our investigation depending on the orientation of the magnetic structures. Flux tubes are, on average, aligned with the Parker spiral direction at 1 AU (Borovsky 2008) showing a median diameter of $\approx$85 R_E comparable to the smaller flux ropes reported by Hu et al. (2018) and the small PDSs reported in Table 2. Feng et al. (2008) reported a uniform orientation distribution in the ecliptic plane for small-scale flux ropes. In contrast, using a larger dataset, Hu et al. (2018) showed that flux ropes manifested an alignment with the Parker spiral. The majority of the reported flux ropes show diameters of $\approx$230–582 R_E (Feng et al. 2008; Cartwright & Moldwin 2010; Yu et al. 2016; Hu et al. 2018) comparable to the azimuthal size scales reported in this study (Table 2). If aligned with the Parker spiral, the azimuthal length scale reported in this study could be a result of the magnetic structures orientation (see Figure 12 in Borovsky (2008) and dependence on IMF clock angle in Dalin et al. (2002)) or due to a correlation scale along the ambient magnetic field (Dalin et al. 2002; Cuesta et al. 2022). Additionally, limitations in the direction perpendicular to the Sun-Earth line could be an inherent property of magnetic features when they are generated at the Sun (see Figure 3–4 in Higginson & Lynch 2018). Interestingly, the features described in Higginson & Lynch (2018) share properties with our PDSs and the features reported by Crooker et al. (1982), that is flattened structures, absence of core IMF, and high plasma beta values. Note also that reconnection at the helmet streamer creates many mesoscale structures (Viall & Vourlidas 2015; Sánchez-Díaz et al. 2017), but only some structures are associated with proper flux ropes (Kepko et al. 2016; Di Matteo et al. 2019b).

Even though we used strict criteria and our statistics have high significance, future studies involving more events and more spacecraft are necessary to rule out any possible dependencies on the small number of events in our dataset and test our estimates of the PDSs' azimuthal scale. Additionally, our results are still dependent on the time delay estimation between spacecraft pair observations, hence future analysis would benefit from reinterpretation in the context of space-time analysis (e.g., Matthaeus et al. 2019). These studies would allow to investigate some questions left open in this work, namely, the association of coherent and not-coherent PDSs with: (i) flux ropes/flux tubes; (ii) n_α/n_p ratio variation; (iii) plasma β and pressure balance conditions; (iv) the different spatial correlation falls off for the IMF intensity and solar wind density.

6. CONCLUSIONS

We investigated the azimuthal size scale of PDSs in high density slow solar wind streams using density and IMF intensity observations at Wind and ARTEMIS-P1, for the first time constraining their azimuthal size scale and the associated IMF variations. The identified PDS time intervals manifest enhancements in the power spectra at certain

Table 2. Size scale estimates for the two main PDS groups.

Parameter	L_x [R_E]	L_C [R_E]	L_T [R_E]	L_y [R_E]	L_x [Mm]	L_C [Mm]	L_T [Mm]	L_y [Mm]
n_p, n_i	86^{+74}_{-37}	294 ± 39	23 ± 14	340 ± 67	551^{+470}_{-237}	1873 ± 248	147 ± 89	2166 ± 427
$\|B\|$	88^{+64}_{-35}	256 ± 43	35 ± 18	326 ± 79	564^{+407}_{-228}	1631 ± 274	223 ± 115	2077 ± 503
n_p, n_i	35^{+28}_{-15}	135 ± 30	26 ± 13	187 ± 56	222^{+179}_{-98}	860 ± 191	166 ± 83	1191 ± 357
$\|B\|$	34^{+34}_{-14}	144 ± 45	27 ± 21	198 ± 87	215^{+221}_{-87}	918 ± 287	172 ± 134	1261 ± 554

NOTE—Median value and absolute uncertainty of the observed PDS radial length scales (L_x) and simulation-inferred core (L_C), tail (L_T), and azimuthal (L_y) PDS scales. Different upper and lower uncertainty for L_x reflect the skewness of the observed distribution.

time scales (converted to radial length scales under the Taylor hypothesis) beyond what can likely be attributed to turbulent or random fluctuations. For each specific radial length scale, we used coherence analysis between spacecraft pair to investigate the PDSs' spatial extent in the direction perpendicular to the Sun-Earth line. Statistical analysis of our dataset comprising 68 high density slow solar wind intervals showed a number of significant results as summarized below:

- The frequency distributions for both solar wind density and IMF intensity manifested the highest occurrence of events at ≈0.5–0.8 mHz. Additional local enhancements appeared centered at ≈1.9 mHz, more evident in the Wind observations for both solar wind parameters, and with more variability within ≈2.7–2.9 mHz and ≈3.2–3.8 mHz. These values correspond to characteristic radial length scales from ≈10 to ≈160 R_E.

- The occurrence of PDSs with high coherence (> 0.7) at similar frequency is higher at low frequencies ($f \leq 1.0$ mHz) and progressively decrease until frequency values of ≈2.8 mHz.

- Occurrence rate distributions for coherent solar wind parcels at specific time/spatial scales (e.g., PDS intervals, especially at $1.0 < f < 2.5$ mHz) further support dependence on separations perpendicular to the Sun-Earth line (Dalin et al. 2002).

- We developed a simple forward model providing estimates of the PDS azimuthal scales. Based on solar wind density, for two classes of events at radial length scales of 86^{+74}_{-37} R_E and 35^{+28}_{-15} R_E, we obtain order of magnitude for the azimuthal length scales of 340 ± 67 R_E and 187 ± 56 R_E, respectively.

Shedding new light on the azimuthal size scale of PDSs is crucial: (i) to constrain any modeling effort trying to explain the origin of these mesoscale structures (Viall et al. 2021) and (ii) to correctly represent the Earth's magnetosphere response to the impact of PDSs (Collier et al. 2000; Weimer et al. 2002; Borovsky, J. E. 2016; Burkholder et al. 2020; Lockwood 2022; Villante et al. 2022; Di Matteo & Sivadas 2022). Even though currently there are limited datasets (especially involving multi-spacecraft observations) which allow to investigate 3D size scale of solar wind mesoscale structures, future studies should involve a larger PDS database and other spacecraft pairs enabling the investigation of larger spatial separation than the one discussed here. This type of analysis will become more feasible in the next decade in light of promising planned and proposed multi-spacecraft missions aimed at better understanding mesoscale structures in the solar wind, e.g., Interplanetary Mesoscale Observatory (InterMeso; Allen et al. 2022), Plasma Observatory (Retinò et al. 2022), Space Weather Investigation Frontier (SWIFT; Akhavan-Tafti et al. 2023), and the Seven Sisters mission (Nykyri et al. 2023).

The authors thank the National Space Science Data Center of the Goddard Space Flight Center for the use permission of Wind and THEMIS data and the NASA CDAWeb team for making these data available (http://cdaweb.gsfc.nasa.gov/istp_public/). The THEMIS program was supported by NASA under contract NAS5-02099. S. D. was supported by NASA Grant 80NSSC21K0459. The work of C. K., N. V., and L. K was supported by the Goddard Space Flight Center Heliophysics Internal Scientist Funding Model (ISFM; competitive work package). All authors would like to thank David Sibeck and Rohit Chibber for useful inputs that have improved the quality of the paper.

Facilities: Wind (SWE, MFI), ARTEMIS-P1 (ESA, FGM)

Software: SPD_MTM (Di Matteo et al. 2020), SPEDAS (Angelopoulos et al. 2019)

REFERENCES

Akhavan-Tafti, M., Johnson, L., Sood, R., et al. 2023, Frontiers in Astronomy and Space Sciences, 10, 1185603, doi: 10.3389/fspas.2023.1185603

Allen, R. C., Smith, E. J., Anderson, B. J., et al. 2022, Front. Astron. Space Sci., doi: 10.3389/fspas.2022.1002273

Alzate, N., Morgan, H., Viall, N., & Vourlidas, A. 2021, ApJ, 919, 98, doi: 10.3847/1538-4357/ac10ca

Angelopoulos, V., Cruce, P., Drozdov, A., et al. 2019, SSRv, 215, 9, doi: 10.1007/s11214-018-0576-4

Auster, H. U., Glassmeier, K. H., Magnes, W., et al. 2008, SSRv, 141, 235, doi: 10.1007/s11214-008-9365-9

Borovsky, J. E. 2008, J. Geophys. Res., 113, A08110, doi: 10.1029/2007JA012684

—. 2022, Frontiers in Astronomy and Space Sciences, 9, 917163, doi: 10.3389/fspas.2022.917163

Borovsky, J. E. 2016, in Space Weather Fundamentals, ed. G. V. Khazanov (CRC Press), doi: 10.1201/9781315368474

Burkholder, B. L., Nykyri, K., & Ma, X. 2020, J. Geophys. Res., 125, e27978, doi: 10.1029/2020JA027978

Cartwright, M. L., & Moldwin, M. B. 2010, J. Geophys. Res., 115, A08102, doi: 10.1029/2009JA014271

Chang, S. C., & Nishida, A. 1973, Ap&SS, 23, 301, doi: 10.1007/BF00645159

Collier, M. R., Szabo, A., Slavin, J. A., Lepping, R. P., & Kokubun, S. 2000, Int. j. geomagn. aeron., 2, 3

Crooker, N. U., Burton, M. E., Phillips, J. L., Smith, E. J., & Balogh, A. 1996, J. Geophys. Res., 101, 2467, doi: 10.1029/95JA03148

Crooker, N. U., Siscoe, G. L., Russell, C. T., & Smith, E. J. 1982, J. Geophys. Res., 87, 2224, doi: 10.1029/JA087iA04p02224

Cuesta, M. E., Chhiber, R., Roy, S., et al. 2022, ApJL, 932, L11, doi: 10.3847/2041-8213/ac73fd

Dalin, P., Zastenker, G., Paularena, K., & Richardson, J. 2002, Journal of Atmospheric and Solar-Terrestrial Physics, 64, 737, doi: 10.1016/S1364-6826(02)00035-4

DeForest, C. E., Howard, R. A., Velli, M., Viall, N., & Vourlidas, A. 2018, ApJ, 862, 18, doi: 10.3847/1538-4357/aac8e3

Di Matteo, S., & Sivadas, N. 2022, Front. Astron. Space Sci., 9, 333, doi: 10.3389/fspas.2022.1060072

Di Matteo, S., Viall, N., & Kepko, L. 2020, SPD_MTM: a spectral analysis tool for the SPEDAS framework, 1.0, Zenodo, doi: 10.5281/zenodo.3703168

Di Matteo, S., Viall, N. M., & Kepko, L. 2021, J. Geophys. Res., 126, doi: 10.1029/2020ja028748

Di Matteo, S., Viall, N. M., Kepko, L., & Villante, U. 2019a, Nuovo Cimento C Geophysics Space Physics C, 42, 20, doi: 10.1393/ncc/i2019-19020-3

Di Matteo, S., Viall, N. M., Kepko, L., et al. 2019b, J. Geophys. Res., 124, 837, doi: 10.1029/2018JA026182

Di Matteo, S., & Villante, U. 2017, Journal of Geophysical Research (Space Physics), 122, 4905, doi: 10.1002/2017JA023936

Di Matteo, S., Villante, U., Viall, N., Kepko, L., & Wallace, S. 2022, J. Geophys. Res., 127, doi: 10.1029/2021ja030144

Feng, H. Q., Wu, D. J., Lin, C. C., et al. 2008, J. Geophys. Res., 113, A12105, doi: 10.1029/2008JA013103

Gershkovich, I., Lepri, S., Viall, N., Di Matteo, S., & Kepko, L. 2023, SoPh, 298, 89, doi: 10.1007/s11207-023-02176-9

Gershkovich, I., Lepri, S. T., Viall, N. M., Di Matteo, S., & Kepko, L. 2022, ApJ, 933, 198, doi: 10.3847/1538-4357/ac73ee

Grinsted, A., Moore, J. C., & Jevrejeva, S. 2004, Nonlinear Processes in Geophysics, 11, 561, doi: 10.5194/npg-11-561-2004

Higginson, A. K., & Lynch, B. J. 2018, ApJ, 859, 6, doi: 10.3847/1538-4357/aabc08

Hu, Q., Zheng, J., Chen, Y., le Roux, J., & Zhao, L. 2018, ApJS, 239, 12, doi: 10.3847/1538-4365/aae57d

Janvier, M., Démoulin, P., & Dasso, S. 2014, SoPh, 289, 2633, doi: 10.1007/s11207-014-0486-x

Katsavrias, C., Hillaris, A., & Preka-Papadema, P. 2016, ASR, 57, 22342244, doi: 10.1016/j.asr.2016.03.001

Katsavrias, C., Papadimitriou, C., Aminalragia-Giamini, S., et al. 2021a, Ann. Geophys., 39, 413, doi: 10.5194/angeo-39-413-2021

Katsavrias, C., Papadimitriou, C., Hillaris, A., & Balasis, G. 2022, Atmos., 13, 499, doi: 10.3390/atmos13030499

Katsavrias, C., Raptis, S., Daglis, I. A., et al. 2021b, Geophys. Res. Lett., 48, doi: 10.1029/2021gl093611

Kepko, L., & Viall, N. M. 2019, Journal of Geophysical Research (Space Physics), 124, 7722, doi: 10.1029/2019JA026962

Kepko, L., Viall, N. M., Antiochos, S. K., et al. 2016, Geophys. Res. Lett., 43, 4089, doi: 10.1002/2016gl068607

Kepko, L., Viall, N. M., & DiMatteo, S. 2024, Journal of Geophysical Research (Space Physics), 129, e2023JA031403, doi: 10.1029/2023JA031403

Kepko, L., Viall, N. M., & Wolfinger, K. 2020, J. Geophys. Res., 125, e28037, doi: 10.1029/2020JA028037

Lavraud, B., Fargette, N., Réville, V., et al. 2020, The Astrophysical Journal, 894, L19, doi: 10.3847/2041-8213/ab8d2d

Lepping, R. P., Acũna, M. H., Burlaga, L. F., et al. 1995, SSRv, 71, 207, doi: 10.1007/bf00751330

Lockwood, M. 2022, Space Weather, 20, e2021SW002989, doi: 10.1029/2021SW002989

Lugaz, N., Zhuang, B., Scolini, C., et al. 2024, The Astrophysical Journal, 962, 193, doi: 10.3847/1538-4357/ad17b9

Matsui, H., Farrugia, C. J., & Torbert, R. B. 2002, J. Geophys. Res., 107, 1355, doi: 10.1029/2002JA009251

Matthaeus, W. H., Dasso, S., Weygand, J. M., et al. 2005, PhRvL, 95, 231101, doi: 10.1103/PhysRevLett.95.231101

Matthaeus, W. H., Bandyopadhyay, R., Brown, M. R., et al. 2019, arXiv e-prints, arXiv:1903.06890. https://arxiv.org/abs/1903.06890

McFadden, J. P., Carlson, C. W., Larson, D., et al. 2008, SSRv, 141, 277, doi: 10.1007/s11214-008-9440-2

Moldwin, M. B., Ford, S., Lepping, R., Slavin, J., & Szabo, A. 2000, Geophys. Res. Lett., 27, 57, doi: 10.1029/1999GL010724

Murphy, A. K., Winslow, R. M., Schwadron, N. A., et al. 2020, The Astrophysical Journal, 894, 120, doi: 10.3847/1538-4357/ab8821

Nykyri, K., Ma, X., Burkholder, B., et al. 2023, Front. Astron. Space Sci., 10, 1179344, doi: 10.3389/fspas.2023.1179344

Ogilvie, K. W., Chornay, D. J., Fritzenreiter, R. J., et al. 1995, SSRv, 71, 55, doi: 10.1007/bf00751326

Paularena, K. I., Zastenker, G. N., Lazarus, A. J., & Dalin, P. A. 1998, J. Geophys. Res., 103, 14601, doi: 10.1029/98JA00660

Pecora, F., Servidio, S., Greco, A., & Matthaeus, W. H. 2021, A&A, 650, A20, doi: 10.1051/0004-6361/202039639

Poirier, N., Réville, V., Rouillard, A. P., Kouloumvakos, A., & Valette, E. 2023, A&A, 677, A108, doi: 10.1051/0004-6361/202347146

Retinò, A., Khotyaintsev, Y., Le Contel, O., et al. 2022, Exp. Astron., 54, 427, doi: 10.1007/s10686-021-09797-7

Richardson, J. D., & Paularena, K. I. 2001, J. Geophys. Res., 106, 239, doi: 10.1029/2000JA000071

Réville, V., Velli, M., Rouillard, A. P., et al. 2020, The Astrophysical Journal, 895, L20, doi: 10.3847/2041-8213/ab911d

Sánchez-Díaz, E., Rouillard, A. P., Davies, J. A., et al. 2017, ApJ, 851, 32, doi: 10.3847/1538-4357/aa98e2

Slepian, D. 1978, Bell Syst. tech. j., 57, 1371, doi: 10.1002/j.1538-7305.1978.tb02104.x

Thomson, D. 1982, Proc. IEEE, 70, 1055, doi: 10.1109/proc.1982.12433

Ventura, R., Antonucci, E., Downs, C., et al. 2023, A&A, 675, A170, doi: 10.1051/0004-6361/202346623

Viall, N. M., DeForest, C. E., & Kepko, L. 2021, Front. Astron. Space Sci., 8, doi: 10.3389/fspas.2021.735034

Viall, N. M., Kepko, L., & Spence, H. E. 2008, J. Geophys. Res., 113, doi: 10.1029/2007JA012881

Viall, N. M., Kepko, L., & Spence, H. E. 2009a, J. Geophys. Res., 114, doi: 10.1029/2008JA013334

Viall, N. M., Spence, H. E., & Kasper, J. 2009b, Geophys. Res. Lett., 36, L23102, doi: 10.1029/2009GL041191

Viall, N. M., Spence, H. E., Vourlidas, A., & Howard, R. 2010, SoPh, 267, 175, doi: 10.1007/s11207-010-9633-1

Viall, N. M., & Vourlidas, A. 2015, ApJ, 807, 176, doi: 10.1088/0004-637x/807/2/176

Villante, U., Recchiuti, D., & Di Matteo, S. 2022, Frontiers in Astronomy and Space Sciences, 9, 835539, doi: 10.3389/fspas.2022.835539

Wang, J., Chhiber, R., Roy, S., et al. 2024, arXiv e-prints, arXiv:2402.05191, doi: 10.48550/arXiv.2402.05191

Weimer, D. R., Ober, D. M., Maynard, N. C., et al. 2002, J. Geophys. Res., 107, 1210, doi: 10.1029/2001JA009102

Weimer, D. R., Ober, D. M., Maynard, N. C., et al. 2003, J. Geophys. Res., 108, 1026, doi: 10.1029/2002JA009405

Wicks, R. T., Chapman, S. C., & Dendy, R. O. 2009, ApJ, 690, 734, doi: 10.1088/0004-637X/690/1/734

Yu, W., Farrugia, C. J., Galvin, A. B., et al. 2016, J. Geophys. Res., 121, 5005, doi: 10.1002/2016JA022642